Elastic and quasi-elastic electron scattering off nuclei with neutron excess

Andrea Meucci, Matteo Vorabbi, Carlotta Giusti, and Franco Davide Pacati
Dipartimento di Fisica, Università degli Studi di Pavia and INFN, Sezione di Pavia, via Agostino Bassi 6, I-27100 Pavia, Italy

Paolo Finelli
Dipartimento di Fisica e Astronomia, Università degli Studi di Bologna and INFN, Sezione di Bologna, via Irnerio 46, I-40126 Bologna, Italy
(Received 14 February 2013; revised manuscript received 29 April 2013; published 28 May 2013)

We present theoretical predictions for electron scattering on oxygen and calcium isotopic chains. The calculations are done within the framework of the distorted-wave Born approximation and the proton and neutron density distributions are evaluated adopting a relativistic Dirac-Hartree model. We present results for the elastic and quasi-elastic cross sections and for the parity-violating asymmetry. As a first step, the results of the models are tested in comparison with some of the data available for elastic and quasi-elastic scattering on ^{16}O and ^{40}Ca nuclei. Then, the evolution of some nuclear properties is investigated as a function of the neutron number. We also present a comparison with the parity-violating asymmetry parameter obtained by the PREX Collaboration on ^{208}Pb and give a prediction for the future experiment CREX on ^{48}Ca.

DOI: 10.1103/PhysRevC.87.054620 PACS number(s): 21.60.Jz, 21.10.−k, 25.30.Fj, 24.10.Jv

I. INTRODUCTION

The nuclear response to an external probe is a powerful tool for investigating the structure of hadron systems such as atomic nuclei and their constituents. In particular, electron-scattering reactions have provided the most complete and detailed information on nuclear and nucleon structure [1–6]. Electrons interact with nuclei predominantly through the electromagnetic interaction, which is well known from quantum electrodynamic and is weak compared with the strength of the interaction between hadrons. The scattering process is therefore adequately treated assuming the validity of the Born approximation, i.e., the one-photon exchange mechanism between electron and target. The virtual photon, like the real one, has a mean free path much larger than the target dimensions, thus exploring the whole target volume. This contrasts with hadron probes, which are generally absorbed at the target surface. Moreover, the ability to vary independently the energy ω and momentum $\boldsymbol{q}$ of the exchanged virtual photon transferred to the nucleus makes it possible to map the nuclear response as a function of its excitation energy with a spatial resolution that can be adjusted to the scale of processes that need to be studied.

Several decades of experimental and theoretical work on electron scattering have provided a wealth of information on the properties of stable nuclei. Nuclear charge density distributions and charge radii have been determined from the analysis of elastic electron-scattering data [7,8]. At low energy loss bound nucleons may produce excited states as a result of single-particle (s.p.) transitions and/or collective motion. Spectroscopic analysis of such excitation mechanisms is the traditional field of nuclear physics. The systematic investigation of inelastic electron scattering has given the necessary support to the foundation of many-body theories applied to the nuclear systems. Spin, parities, and the strength and structure of the transition densities connecting the ground and excited states have been studied [2,9]. In comparison with hadron scattering, which also gives important information, only electron scattering can be used to determine the detailed spatial distributions of the charge transition densities for a variety of s.p. and collective transitions. At energy loss a little above particle emission threshold the quasi-bound giant resonances occur. Here the possibility of independently varying ω and $\boldsymbol{q}$, in conjunction with the coincident detection of nucleons emitted in the decay process, allows a detailed analysis of the various types of collective motions that are responsible for contributions of different multipolarities to such resonances. Several electric and magnetic giant multipole resonances have been discovered and studied using electron scattering [10,11].

At energies above giant resonances a large broad peak occurs at about $\omega = q^2/(2m_N)$, where m_N is the nucleon mass. Its position corresponds to the elastic peak in electron scattering by a free nucleon. It is quite natural to assume that a quasi-free process is responsible for such a peak with a nucleon emitted quasi-elastically. If the nucleons were indeed free, the peak would be sharp and would just occur at $\omega = q^2/(2m_N)$, corresponding to the energy taken by the recoiling free nucleon. A shift in the position of the peak is produced by the nuclear binding, while a broadening of the peak is produced by Fermi motion.

Coincidence $(e, e'p)$ experiments in the quasi-elastic (QE) region represent a very clean tool for exploring the proton-hole states. A large amount of data for the exclusive $(e, e'p)$ reaction has confirmed the assumption of a direct knockout mechanism and has provided accurate information on the s.p. structure of stable closed-shell nuclei [4,5,12–17]. The separation energy and the momentum distribution of the removed proton, which makes it possible to determine the associated quantum numbers, have been obtained. From the comparison between experimental and theoretical cross sections it has been possible to extract the spectroscopic factors, which give a measurement of the occupation of the different shells and, as a consequence, of the effects of nuclear correlations, which go beyond a mean-field description of nuclear structure.

In the inclusive (e, e') process only the scattered electron is detected and the final nuclear state is undetermined, but the

main contribution in the region of the QE peak still comes from the interaction on single nucleons. In comparison with the exclusive $(e, e'p)$ process, the inclusive (e, e') scattering corresponds to an integral over all available nuclear states and consequently provides less specific information, but it is more directly related to the dynamics of the initial nuclear ground state. The width of the QE peak can give a direct measurement of the average momentum of nucleons in nuclei; the shape depends on the distribution in energy and momentum of the initially bound nucleons. Precise measurements can give direct access to integrated properties of the nuclear spectral function that describes this distribution. A considerable body of QE data for light-to-heavy nuclei in different kinematic situations has been collected [5,6,18]. Not only differential cross sections, but also the contribution of the separate longitudinal and transverse response functions, have been considered. From the theoretical point of view, many efforts have been devoted to the description of the available data and important progress has been achieved in terms of experimental results and theoretical understanding [4–6].

The use of the electron probe can be extended to exotic nuclei. The detailed study of the properties of nuclei far from the stability line and the evolution of nuclear properties with respect to the asymmetry between the number of neutrons and protons is one of the major topics of interest in modern nuclear physics.

In the next years the advent of radioactive ion beam (RIB) facilities [19–21] will provide a large amount of data on unstable nuclei. A new generation of electron-RIB colliders using storage rings is under construction at RIKEN (Japan) [22–24] and GSI (Germany) [25]. These facilities will offer unprecedented opportunities to study the structure of exotic unstable nuclei through electron scattering in the ELISe experiment at FAIR in Germany [26–28] and the SCRIT project in Japan [29,30]. Kinematically complete experiments, where, in contrast to conventional electron scattering, all targetlike reaction products are detected, will become feasible for the first time, allowing a clean separation of different reaction channels as well as a reduction of the unavoidable radiative background seen in conventional experiments. Therefore, even applications using stable isotope beams will be of interest.

Several papers devoted to theoretical treatments of electron scattering off exotic nuclei have recently been published, highlighting the usefulness of electron scattering for investigating the structure of unstable nuclei [31–48]. In this work we give another contribution to this field. Here we present and discuss numerical predictions for elastic and inclusive QE electron scattering cross sections on oxygen ($^{14-28}$O) and calcium ($^{36-56}$Ca) isotopic chains.

The study of the evolution of nuclear properties along isotopic chains requires a good knowledge of nuclear-matter distributions for protons and neutrons separately. The ground-state densities reflect the basic properties of effective nuclear forces and provide fundamental nuclear structure information. Elastic electron scattering makes it possible to measure with excellent precision only charge densities and therefore proton distributions. It is much more difficult to measure neutron distributions. Our present knowledge of neutron densities comes primarily from hadron-scattering experiments, the analysis of which requires always model-dependent assumptions about strong nuclear forces at low energies. A model-independent probe of neutron densities is provided by parity-violating elastic electron scattering, where direct information on the neutron density can be obtained from the measurement of the parity-violating asymmetry $A_{\rm pv}$ parameter, which is defined as the difference between the cross sections for the scattering of right- and left-handed longitudinally polarized electrons [49–51]. This quantity is related to the radius of the neutron distribution R_n, because Z^0-boson exchange, which mediates the weak neutral interaction, couples mainly to neutrons and provides a robust model-independent measurement of R_n.

In 2012, the first measurement of $A_{\rm pv}$ [52] (and weak charge form factor [53]) in the elastic scattering of polarized electrons from ^{208}Pb was performed in Hall A at the Jefferson Lab (experiment PREX). The PREX collaboration obtained $A_{\rm pv} = 0.656 \pm 0.060\,(\text{stat}) \pm 0.014\,(\text{syst})$ ppm, corresponding to a difference between the radii of the neutron and proton distributions $R_n - R_p = 0.33^{+0.16}_{-0.18}$ fm. Unfortunately, with such large uncertainties it is not possible to draw definite conclusions about the radius and the distribution of neutrons in a heavy finite nucleus such as ^{208}Pb. The problems that affected the original setup will be strongly reduced by improving electronics and radiation protection (see the recently approved PREX-II experiment [54]). In addition, the CREX experiment [55], with the goal of measuring the neutron skin of ^{48}Ca, has also been conditionally approved. The combined analysis of the PREX and CREX experiments will make it possible to test the assumptions of microscopic models by testing the dependence of R_n on the atomic mass number A.

From a theoretical point of view, parity violation in elastic electron scattering has been recently studied by several authors within the framework of mean-field approaches [43–46,56–59] after almost a decade from the first detailed calculations [51,60,61]. In particular, in Ref. [58] the authors suggested that a 1% measurement of $A_{\rm pv}$ can constrain the slope L of the symmetry energy close to a 10-MeV level of accuracy. A precise measurement of R_n is definitely a crucial step to improve our knowledge of neutron-rich matter, i.e., the outer part of neutron stars.

In this paper we present calculations of $A_{\rm pv}$ performed for oxygen and calcium isotopic chains and test the isotopic dependence. In addition, we present a comparison with the results of the PREX collaboration and provide some estimates for the future experiment CREX.

The basic ingredients of the calculations for both elastic and QE scattering are the ground-state wave functions of proton and neutron s.p. states, for which we have used a relativistic mean-field (RMF) model. In recent years mean-field approaches have been very successfully employed in several aspects of nuclear structure phenomena. Effective hadron field theories with medium-dependent parametrizations of the meson-nucleon vertices retain the basic structure of the RMF framework, but can be more directly related to the underlying microscopic description of nuclear interactions [62–64]. After the first applications [65,66], restricted to infinite systems and spherical nuclei, with the parametrizations DD-ME1 [67] and DD-ME2 [68], calculations have been extended to open-shell

nuclei, exotic systems, superheavies, and collective resonances [69].

The cross sections for elastic electron scattering are obtained from the numerical solution of the partial-wave Dirac equation and includes Coulomb distortion effects.

In inclusive QE electron scattering a proper description of the final-state interactions (FSIs) between the emitted nucleon and the residual nucleus is an essential ingredient for the comparison with data. For the calculations presented in this paper we have employed the relativistic Green's function model, which has been widely and successfully applied to the analysis of QE electron and neutrino-nucleus scattering data on different nuclei [70–77].

As a first step, we test the results of the models in comparison with some of the data available for elastic and QE scattering on ^{16}O and ^{40}Ca nuclei. Then, with extensive calculations on oxygen and calcium isotopic chains, we investigate the evolution of some ground-state properties as a function of the neutron number.

The case of the exclusive quasi-free $(e, e'p)$ reaction has been investigated in Refs. [47,78], where the cross sections obtained with different relativistic and nonrelativistic approaches based on the mean-field description for the proton bound-state wave function are compared for oxygen and calcium isotopic chains.

The paper is organized as follows. In Sec. II we give the basic formalism involved in the description of elastic, QE, and parity-violating electron scattering. In Sec. III we present a brief discussion of the RMF model and of the calculations of the self-consistent ground-state proton and neutron densities of calcium and oxygen isotopes. In Sec. IV we outline the main features of the relativistic Green's function model, which is used to describe FSIs in the inclusive QE electron scattering. In Sec. V we show and discuss our theoretical results obtained for elastic, QE, and parity-violating electron scattering. Finally, in Sec. VI we summarize our results and present our conclusions.

II. ELASTIC AND QUASI-ELASTIC ELECTRON SCATTERING

A. Elastic electron scattering

In the one-photon exchange approximation and neglecting the effect of the nuclear Coulomb field on incoming and outgoing electrons, i.e., in the plane-wave Born approximation (PWBA), the differential cross section for the elastic scattering of an electron with momentum transfer q off a spherical spin-zero nucleus is given by

$$\left(\frac{d\sigma}{d\Omega'}\right)_{EL} = \sigma_M F_p(q)^2, \tag{1}$$

where Ω' is the scattered electron solid angle, σ_M is the Mott cross section [4,5], and

$$F_p(q) = \int d\mathbf{r} j_0(qr)\rho_p(r) \tag{2}$$

is the charge form factor for a spherical nuclear charge (point proton) density $\rho_p(r)$ and j_0 is the zeroth-order spherical Bessel function.

The PWBA is, however, not adequate for medium and heavy nuclei where the distortion produced on the electron wave functions by the nuclear Coulomb potential $V(r)$ from $\rho_p(r)$ can have significant effects. The DWBA cross sections are obtained from the numerical solutions of the partial-wave Dirac equation.

B. Inclusive quasi-elastic electron scattering

In the one-photon exchange approximation the inclusive differential cross section for the QE (e, e') scattering on a nucleus is obtained from the contraction between the lepton and hadron tensors as [5]

$$\left(\frac{d\sigma}{d\varepsilon' d\Omega'}\right)_{QE} = \sigma_M[v_L R_L + v_T R_T], \tag{3}$$

where ε' is the energy of the scattered electron. The coefficients v come from the components of the lepton tensor that, under the assumption of the plane-wave approximation for the electron wave functions, depend only on the lepton kinematics,

$$v_L = \left(\frac{|Q^2|}{|\boldsymbol{q}|^2}\right)^2, \quad v_T = \tan^2\frac{\theta}{2} - \frac{|Q^2|}{2|\boldsymbol{q}|^2}, \tag{4}$$

where θ is the electron-scattering angle and $Q^2 = |\boldsymbol{q}|^2 - \omega^2$. All nuclear structure information is contained in the longitudinal and transverse response functions R_L and R_T, expressed by

$$\begin{aligned} R_L(q,\omega) &= W^{00}(q,\omega), \\ R_T(q,\omega) &= W^{11}(q,\omega) + W^{22}(q,\omega), \end{aligned} \tag{5}$$

in terms of the diagonal components of the hadron tensor, which is given by bilinear products of the transition matrix elements of the nuclear electromagnetic many-body current operator $\hat{J}^\mu$ between the initial state of the nucleus $|\Psi_0\rangle$, of energy E_0, and the final states $|\Psi_f\rangle$, of energy E_f, both eigenstates of the nuclear Hamiltonian H, as

$$\begin{aligned} W^{\mu\mu}(q,\omega) = \overline{\sum_i} \sum\!\!\!\!\!\!\int_f \langle\Psi_f|\hat{J}^\mu(\boldsymbol{q})|\Psi_0\rangle \\ \times \langle\Psi_0|\hat{J}^{\mu\dagger}(\boldsymbol{q})|\Psi_f\rangle\, \delta(E_0+\omega-E_f), \end{aligned} \tag{6}$$

involving an average over the initial states and a sum over the undetected final states. The sum runs over the scattering states corresponding to all of the allowed asymptotic configurations and includes possible discrete states [4,5].

The hadron tensor can equivalently be expressed as

$$W^{\mu\mu}(q,\omega) = -\frac{1}{\pi}\,\mathrm{Im}\langle\Psi_0|J^{\mu\dagger}(\boldsymbol{q})G(E_f)J^\mu(\boldsymbol{q})|\Psi_0\rangle, \tag{7}$$

where $E_f = E_0 + \omega$ and $G(E_f)$ is the many-body Green's function related to the many-body nuclear Hamiltonian H.

The hadron in tensor in Eq. (7) contains the full many-body propagator of the nuclear system. As such, it is an extremely complicated object and some approximations are needed to reduce the calculation of the nuclear response to a tractable form.

C. Parity-violating electron scattering

When a photon is exchanged between two charged particles a Z^0 boson is also exchanged. At the energies of interest in electron scattering the strength of the weak process mediated by the Z^0 boson is negligible compared with the electromagnetic strength. The role played by the Z^0 exchange is therefore not significant unless an experiment is set up to measure a parity-violating observable. While the electromagnetic interaction conserves parity, the weak interaction does not and this is how we are sensitive to Z^0 exchange in electron scattering.

The degree of parity violation can be measured by the parity-violating asymmetry $A_{\rm pv}$, or helicity asymmetry, which is defined as the difference between the cross sections for the scattering of electrons longitudinally polarized parallel and antiparallel to their momentum. This difference arises from the interference of photon and Z^0 exchange. As it has been shown in Refs. [49,60], the asymmetry in the parity-violating elastic polarized electron scattering represents an almost direct measurement of the Fourier transform of the neutron density.

The electron spinor for elastic scattering on a spin-zero nucleus can be written as the solution of a Dirac equation with total potential

$$U(r) = V(r) + \gamma_5 A(r), \tag{8}$$

where $V(r)$ is the Coulomb potential and $A(r)$ is the axial potential that results from the weak neutral current amplitude and which depends on the Fermi constant $G_F \simeq 1.16639 \times 10^{-11}$ MeV^{-2}, i.e.,

$$A(r) = \frac{G_F}{2\sqrt{2}}\,\rho_W(r). \tag{9}$$

The weak charge density ρ_W is related to the neutron density and it is defined

$$\rho_W(r) = \int \mathrm{d}\mathbf{r}'\, G_E(|\mathbf{r}-\mathbf{r}'|) \times [-\rho_n(r') + (1 - 4\sin^2\Theta_W)\rho_p(r')], \tag{10}$$

where ρ_n and ρ_p are point neutron and proton densities, respectively, $G_E(r) \approx \frac{\Lambda^3}{8\pi}\, e^{-\Lambda r}$ is the electric form factor of the proton, with $\Lambda = 4.27$ fm^{-1}, and $\sin^2\Theta_W \simeq 0.23$ is the Weinberg angle. The axial potential of Eq. (9) is much smaller than the vector potential and, because $1 - 4\sin^2\Theta_W \ll 1$, it depends mainly on the neutron distribution $\rho_n(r)$.

In the limit of vanishing electron mass, the helicity states $\Psi_\pm = \frac{1}{2}(1 \pm \gamma_5)\Psi$ satisfy the Dirac equation

$$[\boldsymbol{\alpha}\cdot\mathbf{p} + U_\pm(r)]\Psi_\pm = E\Psi_\pm, \tag{11}$$

with

$$U_\pm(r) = V(r) \pm A(r). \tag{12}$$

The parity-violating asymmetry $A_{\rm pv}$, or helicity asymmetry, is defined

$$A_{\rm pv} = \frac{\frac{d\sigma_+}{d\Omega} - \frac{d\sigma_-}{d\Omega}}{\frac{d\sigma_+}{d\Omega} + \frac{d\sigma_-}{d\Omega}}, \tag{13}$$

where $+(-)$ refers to the elastic scattering on the potential $U_\pm(r)$. In Born approximation, neglecting strangeness contributions and the electric neutron form factor, the parity-violating asymmetry can be rewritten as [61,79]

$$A_{\rm pv} = \frac{G_F\, Q^2}{4\sqrt{2}\,\pi\alpha}\left[4\sin^2\Theta_W - 1 + \frac{F_n(q)}{F_p(q)}\right]. \tag{14}$$

Because $4\sin^2\Theta_W - 1$ is small and $F_p(q)$ is known, we see that $A_{\rm pv}$ provides a practical method to measure the neutron form factor $F_n(q)$ and hence the neutron radius. For these reasons parity-violating electron scattering (PVES) has been suggested as a clean and powerful tool for measuring the spatial distribution of neutrons in nuclei.

In QE electron scattering the helicity asymmetry is obtained in terms of kinematic coefficients v from the lepton tensor and of nuclear response functions as [72]

$$A_{\rm pv}^{\rm QE} = A_0 \frac{v_L R_L^{\rm AV} + v_T R_T^{\rm AV} + v_T' R_T^{\rm VA}}{v_L R_L + v_T R_T}. \tag{15}$$

The factor A_0 is defined as

$$A_0 = \frac{G_F\, Q^2}{2\sqrt{2}\pi\alpha}, \tag{16}$$

where α is the fine structure constant. The denominator in Eq. (15) contains the parity-conserving cross section of Eq. (3) and the numerator the parity-violating contribution,

$$v_T' = \tan\frac{\theta}{2}\sqrt{\tan^2\frac{\theta}{2} + \frac{Q^2}{|\boldsymbol{q}|^2}}, \tag{17}$$

and the response functions R are given in terms of the polarized components of the hadron tensor $W_I^{\mu\nu}$ [72] as

$$\begin{aligned} R_L^{\rm AV} &= g_A W_I^{00}, \quad R_T^{\rm AV} = g_A\left(W_I^{11} + W_I^{22}\right), \\ R_T^{\rm VA} &= i g_V\left(W_I^{12} - W_I^{21}\right), \end{aligned} \tag{18}$$

where the superscript AV denotes interference of axial-vector leptonic current with vector hadronic current (the reverse for VA) and the couplings $g_A = -\frac{1}{2}$ and $g_V = -\frac{1}{2} + 2\sin^2\Theta_W \simeq -0.04$.

III. RELATIVISTIC MODEL FOR GROUND-STATE OBSERVABLES

In the standard representation of RMF approaches the nucleus is described as a system of Dirac nucleons coupled to the exchange mesons and the electromagnetic field through an effective Lagrangian. The isoscalar scalar-meson (σ), the isoscalar vector-meson (ω), and the isovector vector-meson (ρ) build the minimal set of meson fields that together with the electromagnetic field (γ) is necessary for a quantitative description of bulk and s.p. nuclear properties. The model is defined by the Lagrangian density

$$\mathcal{L} = \mathcal{L}_N + \mathcal{L}_m + \mathcal{L}_{\rm int}, \tag{19}$$

where $\mathcal{L}_N$ denotes the Lagrangian of the free nucleon, $\mathcal{L}_m$ is the Lagrangian of the free meson fields, and the simplest set of interaction terms is contained in $\mathcal{L}_{\rm int}$:

$$\mathcal{L}_{\rm int} = -g_\sigma\bar\psi\sigma\psi - g_\omega\bar\psi\gamma^\mu\omega_\mu\psi - g_\rho\bar\psi\gamma^\mu\vec\tau\cdot\vec\rho_\mu\psi. \tag{20}$$

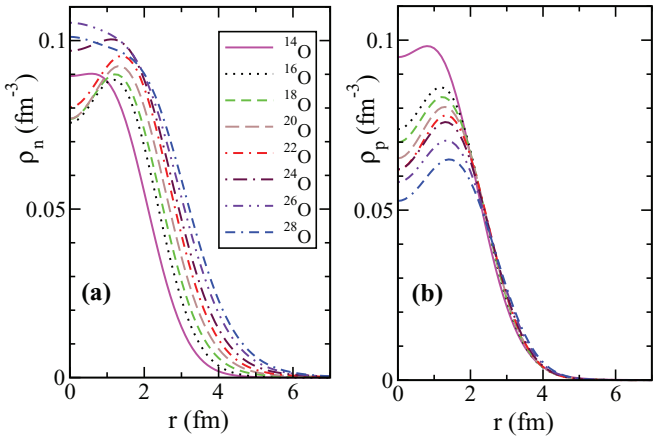

FIG. 1. (Color online) Neutron (a) and proton (b) distributions for the various oxygen isotopes we have considered.

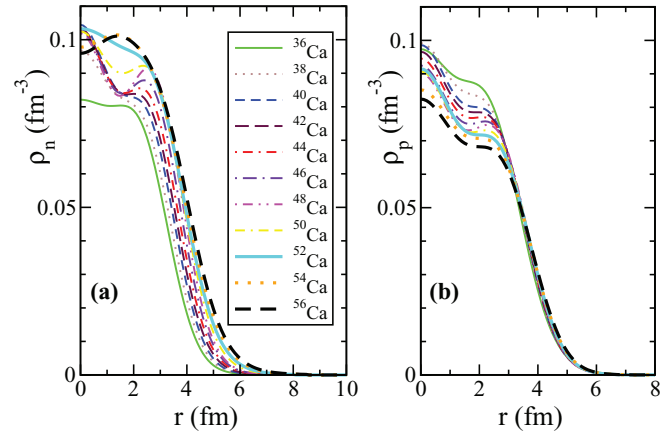

FIG. 2. (Color online) The same as in Fig. 1, but for calcium isotopes.

The couplings of the σ meson and ω meson to the nucleon are assumed to be of the form

$$g_i(\rho) = g_i(\rho_{\rm sat}) f_i(x) \quad \text{for} \quad i = \sigma, \omega, \tag{21}$$

where

$$f_i(x) = a_i \frac{1 + b_i(x + d_i)^2}{1 + c_i(x + d_i)^2} \tag{22}$$

is a function of $x = \rho/\rho_{\rm sat}$ and $\rho_{\rm sat} = 0.152$ fm^{-3} denotes the nucleon density at saturation in symmetric nuclear matter. Constraints at nuclear-matter saturation density and at zero density are used to reduce the number of independent parameters in Eq. (22) to three. Three additional parameters in the isoscalar channel are $g_\sigma(\rho_{\rm sat})$, $g_\omega(\rho_{\rm sat})$, and m_σ, which is the mass of the phenomenological σ meson. For the ρ meson coupling the functional form of the density dependence is suggested by Dirac-Brueckner calculations of asymmetric nuclear matter,

$$g_\rho(\rho) = g_\rho(\rho_{\rm sat}) \exp[-a_\rho(x - 1)], \tag{23}$$

and the isovector channel is parametrized by $g_\rho(\rho_{\rm sat})$ and a_ρ. Bare values are used for the masses of the ω and ρ mesons: $m_\omega = 783$ MeV and $m_\rho = 763$ MeV. DD-ME2 is determined by eight independent parameters, adjusted to the properties of symmetric and asymmetric nuclear matter, binding energies, charge radii, and neutron radii of spherical nuclei [68]. The interaction has been tested in the calculation of ground-state properties of a large set of spherical and deformed nuclei. When used in the relativistic random-phase approximation, DD-ME2 reproduces with high accuracy data on isoscalar and isovector collective excitations. For open-shell nuclei we employed a schematic ansatz: the constant gap approximation with empirical Δ given by the five-point formula [80]

$$\Delta^{(5)}(N_0) = -\tfrac{1}{8}[E(N_0 + 2) - 4E(N_0 + 1) + 6E(N_0) - 4E(N_0 - 1) + E(N_0 - 2)]. \tag{24}$$

In Figs. 1 and 2 we plot the neutron (proton) density distributions $\rho_{n(p)}$ as functions of the radial coordinate r for oxygen and calcium isotopes, respectively. These density distributions are the sum of the squared moduli of the s.p. neutron (proton) wave functions. All the nuclei we have investigated ended up being bound. From the experimental point of view it seems rather well established that the neutron drip line for the oxygen isotopes starts with ^{26}O [81] and, therefore, ^{28}O should not be bound.

For both isotopic chains the differences between the proton and the neutron densities in Figs. 1 and 2 generally increase with the neutron number. When the number of neutrons increases there is a gradual increase of the neutron radius. The differences of the neutron density profiles in the nuclear interior display pronounced shell effects. The effect of adding neutrons is to populate and extend the neutron densities and, to a minor extent, also the proton densities. In the case of protons, however, there is a decrease of the density in the nuclear interior to preserve the normalization to the constant number of protons.

IV. RELATIVISTIC GREEN'S FUNCTION MODEL FOR INCLUSIVE QUASI-ELASTIC ELECTRON SCATTERING

In the QE region the nuclear response is dominated by one-nucleon knockout processes, where the scattering occurs with only one nucleon that is subsequently emitted. The remaining nucleons of the target behave as simple spectators and QE electron scattering can adequately be described in the relativistic impulse approximation (RIA) by the sum of incoherent processes involving only one nucleon scattering and the components of the hadron tensor of Eq. (6) are obtained from the sum, over all the s.p. shell-model states, of the squared absolute value of the transition matrix elements of the single-nucleon current.

A reliable description of FSIs between the ejected nucleon and the residual nucleus is an essential ingredient for the comparison with data. In the case of exclusive $(e, e'p)$ processes, the use of complex optical potentials in the relativistic distorted wave impulse approximation (RDWIA) has been able to successfully describe a wide number of experimental data [16,47,48,82–86]. It is clear that the pure RDWIA approach,

based on the use of an absorptive complex potential, would be inconsistent in the analysis of inclusive scattering, where all final-state channels should be retained and the total flux, although redistributed among all possible channels owing to FSIs, must be conserved. Different approaches have been used to describe FSIs in RIA calculations for the inclusive QE electron- and neutrino-nucleus scattering [70–75,77,87–96]. In the relativistic plane-wave impulse approximation (RPWIA), FSI are simply neglected. In another approach, FSIs are included in calculations where the final nucleon state is evaluated with real potentials, either retaining only the real part of the relativistic energy-dependent complex optical potential (rROP) [95,96] or using the same RMF potential considered in describing the initial nucleon state [91].

In the relativistic Green's function (RGF) model FSIs are described in the inclusive process consistently with the exclusive scattering by the same complex optical potential, but the imaginary part is used in the two cases in a different way and in the inclusive scattering it redistributes the flux in all the channels and the total flux is conserved. Detailed discussions of the RGF model can be found in Refs. [70–77,97,98]. The model assumes that the ground state of the nucleus $|\Psi_0\rangle$ is nondegenerate; this is a suitable approximation for the even isotopes of oxygen and calcium considered in this work, with spin and parity 0^+ [99].

In the RGF model with suitable approximations, which are mainly related to the impulse approximation, the components of the nuclear response of Eq. (7) are written in terms of the s.p. optical model Green's function. The spectral representation of the s.p. Green's function, which is based on a biorthogonal expansion in terms of a non-Hermitian optical potential and of its Hermitian conjugate, can be exploited to avoid the explicit calculation of the s.p. Green's function and obtain the components of the hadron tensor in the form [70]

$$W^{\mu\mu}(q,\omega) = \sum_n \left[\mathrm{Re}\ T_n^{\mu\mu}(E_f-\varepsilon_n, E_f-\varepsilon_n) - \frac{1}{\pi}\mathcal{P} \times \int_M^\infty \mathrm{d}\mathcal{E} \frac{1}{E_f-\varepsilon_n-\mathcal{E}}\ \mathrm{Im}\ T_n^{\mu\mu}(\mathcal{E}, E_f-\varepsilon_n)\right], \quad (25)$$

where $\mathcal{P}$ denotes the principal value of the integral, n is the eigenstate of the residual nucleus with energy ε_n, and

$$T_n^{\mu\mu}(\mathcal{E},E) = \lambda_n \langle \varphi_n | j^{\mu\dagger}(\boldsymbol{q}) \sqrt{1-\mathcal{V}'(E)} | \tilde{\chi}_{\mathcal{E}}^{(-)}(E)\rangle \times \langle \chi_{\mathcal{E}}^{(-)}(E) | \sqrt{1-\mathcal{V}'(E)}\, j^{\mu}(\boldsymbol{q}) | \varphi_n \rangle. \quad (26)$$

The factor $\sqrt{1-\mathcal{V}'(E)}$, where $\mathcal{V}'(E)$ is the energy derivative of the optical potential, accounts for interference effects between different channels and justifies the replacement in the calculations of the Feshbach optical potential $\mathcal{V}$ of the RGF model by the local phenomenological optical potential [70,97,98].

Disregarding the square root correction, the second matrix element in Eq. (26) is the transition amplitude of the usual RDWIA model for the exclusive single-nucleon knockout. In this matrix element j^μ is the one-body nuclear current, $\chi^{(-)}$ is the s.p. scattering state of the emitted nucleon with energy $\mathcal{E}$, φ_n is the overlap between the ground state of the target and the final state n, i.e., a s.p. bound state, and the spectroscopic factor λ_n is the norm of the overlap function. In the model φ_n and $\chi^{(-)}$ are consistently derived as eigenfunctions of the energy-dependent optical-model Hamiltonian at bound and scattering energies.

In the exclusive one-nucleon knockout the imaginary part of the optical potential accounts for the flux lost in the channel n toward the channels different from n, which are not included in the exclusive process. In the inclusive response, where all the channels are included, this loss is compensated by a corresponding gain of flux owing to the flux lost, toward the channel n, in the other final states asymptotically originated by the channels different from n. This compensation is performed by the first matrix element in the right-hand side of Eq. (26), which involves the eigenfunction $\tilde{\chi}_{\mathcal{E}}^{(-)}(E)$ of the Hermitian conjugate optical potential, where the imaginary part has an opposite sign and has the effect of increasing the strength. Therefore, in the RGF approach the imaginary part of the optical potential redistributes the flux lost in a channel in the other channels, and in the sum over n the total flux is conserved. If the imaginary part of the optical potential is neglected, the second term in Eq. (25) vanishes and, but for the square root factor, the first term gives the rROP approach.

In Eq. (26) $\tilde{\chi}^{(-)}$ and $\chi^{(-)}$ are therefore eigenfunctions of the optical potential $\mathcal{V}(E)$ and of its Hermitian conjugate $\mathcal{V}^\dagger(E)$, which are nonlocal operators with a possibly complicated matrix structure. Neither microscopic nor empirical calculations of $\mathcal{V}(E)$ are available. Only phenomenological local optical potentials, obtained through fits to elastic nucleon-nucleus scattering data, are available. These phenomenological optical potentials are used in RGF calculations. As no relativistic optical potentials are available for the bound states, the overlap functions φ_n, are computed in the present work using the model discussed in Sec. III.

The RGF model has been applied to parity-violating QE electron scattering in Ref. [72]. The main steps of the model are the same; the expressions for the electromagnetic-weak interference components of the hadron tensor $W_I^{\mu\nu}$ can be found in Ref. [72].

V. RESULTS

In this section we present and discuss numerical predictions for elastic and QE electron scattering which can hopefully be useful for future measurements in experimental RIB facilities. We study the evolution of some electron-scattering observables in isotopic chains of medium systems, which are exemplified by the cases of the oxygen and calcium isotopes. Many of these nuclei lie in the region of the nuclear chart that is likely to be explored in future electron-scattering experiments. As a first step, with a few numerical examples we test the results of our models in comparison with available data. Then, for each nucleus in an isotopic chain, we compute and compare the associated elastic and QE cross sections and parity-violating asymmetry to obtain information on the effects of isospin asymmetry on nuclear structure.

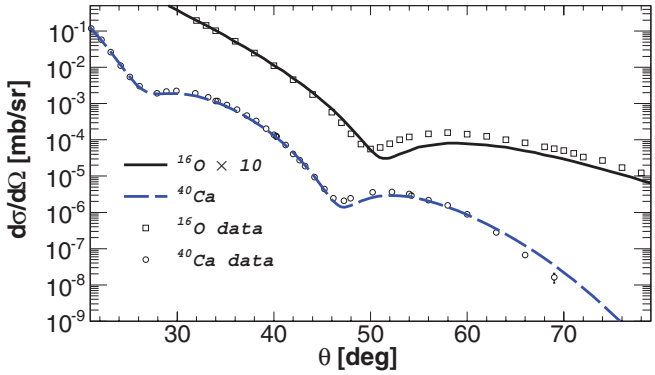

FIG. 3. (Color online) Differential cross section for elastic electron scattering on ^{16}O at an electron energy $\varepsilon = 374.5$ MeV and ^{40}Ca at $\varepsilon = 496.8$ MeV as a function of the scattering angle θ. Experimental data from [111] (^{16}O) and [112] (^{40}Ca).

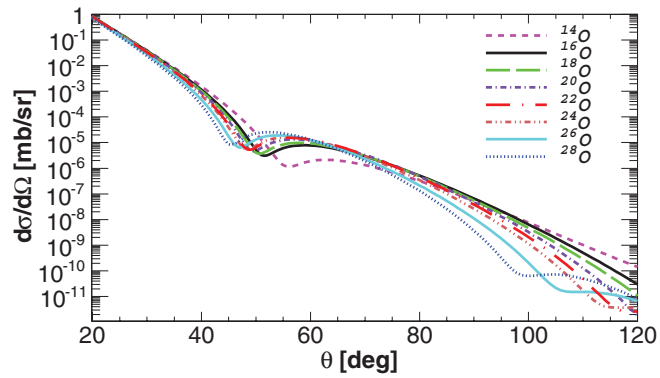

FIG. 4. (Color online) Differential cross section for elastic electron scattering on $^{14-28}$O at $\varepsilon = 374.5$ MeV as a function of θ.

A. Elastic electron scattering

The cross sections for elastic electron scattering have been calculated in the DWBA and with the self-consistent relativistic ground-state charge densities described in Sec. III. In the PWBA the cross section is proportional to the Fourier transform of the proton charge density [see Eq. (2)] and reflects its behavior also when Coulomb distortion is included in the calculations. In different studies of the charge form factors along isotopic chains [36,40,41,100,101] it has been found that, when the number of neutrons increases, the squared modulus of the charge form factor and the positions of its minima show, respectively, an upward trend and a significant inward shifting in the momentum transfer.

An example of the comparison between theoretical and experimental differential cross sections is displayed in Fig. 3 for elastic electron scattering on ^{16}O at an electron energy $\varepsilon = 374.5$ MeV and on ^{40}Ca at $\varepsilon = 496.8$ MeV. The general trend of the experimental data is reasonably reproduced by the calculations. Both experimental cross sections considered in the figure are well described at low scattering angles. For ^{40}Ca there is a fair agreement between theory and data also at larger angles, while for ^{16}O data beyond the minimum are somewhat underestimated by the theoretical results.

The calculated differential cross sections for elastic electron scattering on various oxygen isotopes ($^{14-28}$O) at $\varepsilon = 374.5$ MeV and on calcium isotopes ($^{36-56}$Ca) at $\varepsilon = 496.8$ MeV are shown in Figs. 4 and 5, respectively. With increasing neutron number the positions of the diffraction minima shift toward smaller scattering angles, i.e., toward smaller values of the momentum transfer. The shift of the minima toward smaller q is, in general, accompanied by a simultaneous increase in the height of the maxima. The behavior is similar for both isotopic chains here considered and is in agreement with the results found in previous studies of charge form factors on various isotopic chains, which were carried out with different mean-field models [36,40,41,100,101].

B. Quasi-elastic electron scattering

The cross sections for QE electron scattering have been computed with the RGF model discussed in Sec. IV. Some results obtained in the RPWIA are also presented for a comparison. In the calculations of the matrix elements in Eq. (26) the s.p. bound nucleon states are obtained from the RMF model with density-dependent meson-nucleon vertices and the DD-ME2 parametrization as described in Sec. III. The s.p. scattering states are eigenfunctions of the energy-dependent and A-dependent (A is the mass number) parametrization for the relativistic optical potential of Ref. [102], which is fitted to proton elastic scattering data on several nuclei in an energy range up to 1040 MeV. The different number of neutrons along the O and Ca isotopic chains produces different optical potentials (see Ref. [102] for more details). For the single-nucleon current we have used the relativistic free nucleon expression denoted as CC2 [70,103].

The predictions of the RGF model have been compared with experimental data for QE electron- and neutrino-nucleus scattering in a series of papers [70–77,89,93], where the calculations have been performed with different RMF models for the bound states and different parametrizations of the relativistic optical potential.

In Fig. 6 our RGF results are compared with the experimental (e, e') cross sections for two different kinematics on ^{16}O and ^{40}Ca target nuclei [104,105]. The agreement with the data is satisfactory, at least in the energy region of the QE peak. The RGF model was developed to describe FSI in

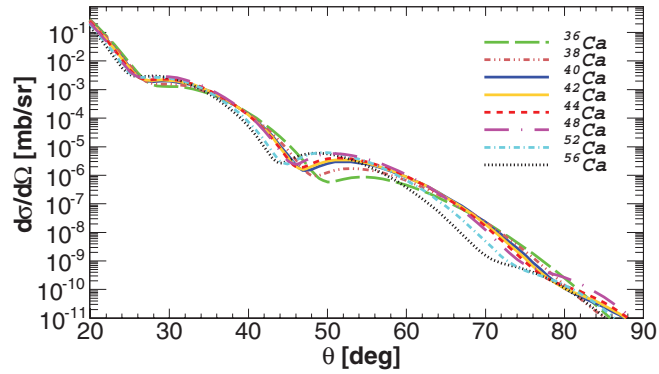

FIG. 5. (Color online) Differential cross section for elastic electron scattering on $^{36-56}$Ca at $\varepsilon = 496.8$ MeV as a function of θ.

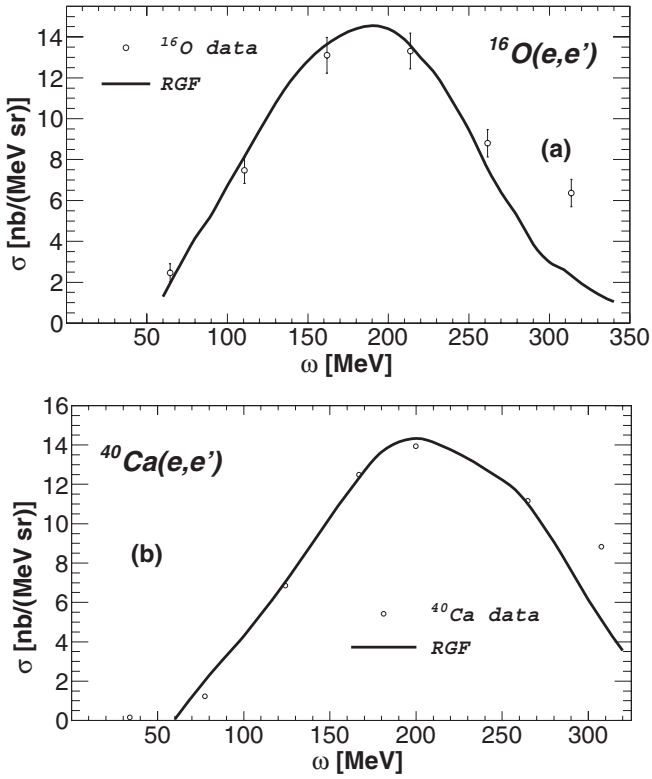

FIG. 6. Differential cross section of the reactions ^{16}O(e, e') (a) and ^{40}Ca(e, e') (b) for different beam energies and electron-scattering angles, $\varepsilon = 1080$ MeV and $\theta = 32^\circ$ for ^{16}O(e, e') and $\varepsilon = 841$ MeV and $\theta = 45.5^\circ$ for ^{40}Ca(e, e'), as a function of the energy transfer ω. The RGF results are compared with the experimental data from [104] [^{16}O(e, e')] and [105] [^{40}Ca(e, e')].

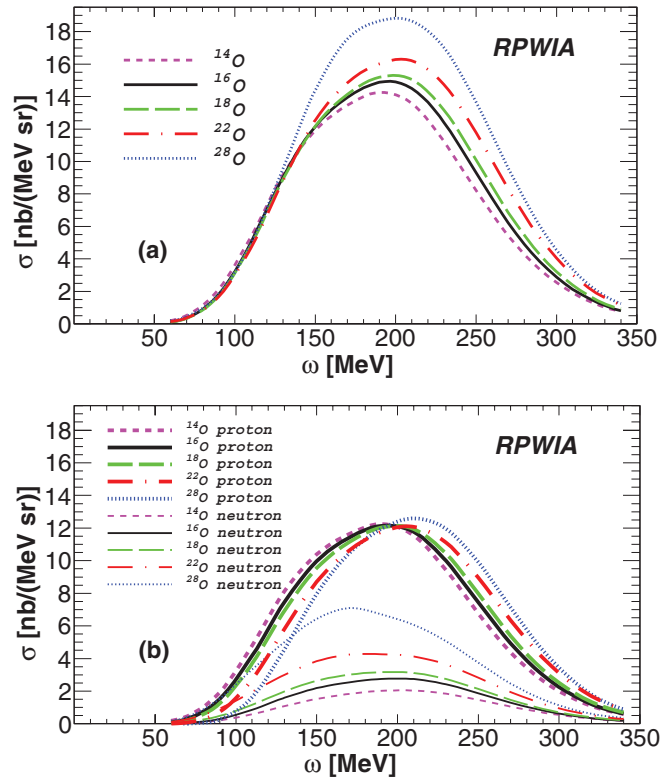

FIG. 7. (Color online) In panel (a) the differential RPWIA cross section for the inclusive QE (e, e') reaction on $^{14-28}$O at $\varepsilon = 1080$ MeV and $\theta = 32^\circ$ is shown as a function of ω. In panel (b) the separate contributions of protons (thick lines) and neutrons (thin lines) are displayed.

inclusive QE electron scattering and is, in general, able to give a reasonable and even good description of QE data. For energy regions below and above the QE peak other contributions, not included in the RGF model, can be important. Even in the QE region, the relevance of contributions such as meson exchange currents and Δ effects should be carefully evaluated before definite conclusions can be drawn about the comparison with data [106–108]. Such contributions may be significant even in the QE region, in particular in kinematics where the transverse component of the nuclear response plays a major role in the cross section.

The cross section of the inclusive QE (e, e') reaction on $^{14-28}$O isotopes at $\varepsilon = 1080$ MeV and $\theta = 32^\circ$ are shown in Fig. 7. In a first approximation, we have neglected FSI and calculations have been performed in the RPWIA. In this case, the differences between the results for the various isotopes are entirely attributable to the differences in the s.p. bound-state wave functions of each isotope. While only the charge proton density distribution contributes to the cross section of elastic electron scattering, the cross section of QE electron scattering is obtained from the sum of all the integrated exclusive one-nucleon knockout processes, owing to the interaction of the probe with all the individual nucleons, protons, and neutrons, of the nucleus and contains information on the dynamics of the initial nuclear ground state. The separate contributions from protons and neutrons are also shown in the bottom panel of Fig. 7. In an usual experiment where only the scattered electron is detected these two quantities cannot be separated experimentally, but their comparison can give useful information on the different role of protons and neutrons in the inclusive QE cross section. The main role is played by protons, which give most of the contribution. Increasing the neutron number it is quite natural to understand the proportional increase of the neutron contribution. No significant increase is found in the proton contribution. Thus, the increase of the cross section in the top panel of the figure is attributable to the increase of the neutron contribution. The shift of the proton contribution toward higher values of ω seen in the figure is more related to the increase of the proton separation energy with increasing neutron number (increasing the neutron number the protons experience more binding and their separation energies increase) than to changes in the proton wave functions. A different and opposite shift can be seen in the case of the neutron contribution and, therefore, the final effect is that the shift is strongly reduced in the QE cross section shown in the top panel of Fig. 7.

In Fig. 8 we show the QE (e, e') cross sections calculated for oxygen isotopes with the RGF model and in the same kinematics as in Fig. 7. The general trend of the cross sections, their magnitude, and their evolution with respect to the change of the neutron number are generally similar in

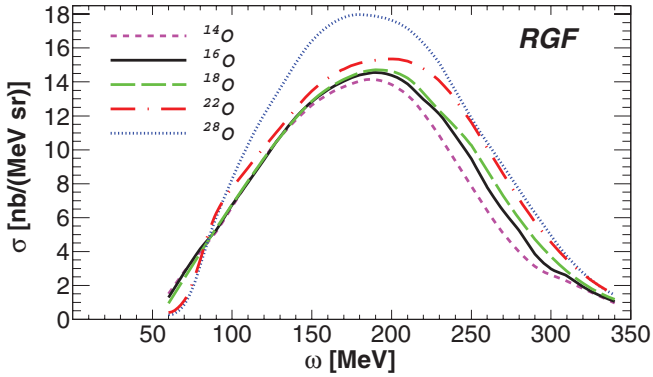

FIG. 8. (Color online) Differential RGF cross section for the inclusive QE (e, e') reaction on $^{14-28}$O in the same kinematics as in Fig. 7.

RPWIA and RGF. The FSI effects in the RGF calculations produce, however, some differences which can be seen in the low energy transferred region, where the cross sections for ^{14,16,18}O are enhanced with respect to those for ^{22}O and ^{28}O. In addition, the shift toward higher ω is more significant than in the RPWIA case, but for ^{28}O.

The cross section of the inclusive QE (e, e') reaction on $^{36-56}$Ca isotopes at $\varepsilon = 560$ MeV and $\theta = 60^\circ$ calculated in the RPWIA and in the RGF are shown in Figs. 9 and 10, respectively. The general behavior of the cross sections and their evolution with increasing neutron number is similar for calcium and oxygen isotopes. The magnitude increases with the neutron number, but FSI effects are somewhat more visible for calcium isotopes. The RGF cross sections on ^{36,40,44,48}Ca in Fig. 10 are enlarged over a wide range of ω and are slightly reduced with respect to the RPWIA results in Fig. 9. This is particularly visible for ^{48}Ca and produces an apparently large gap between the cross sections of ^{48}Ca and ^{52}Ca.

As a final comment, we can add that interesting and peculiar effects are obtained in the evolution of QE inclusive cross section along isotopic chains, but it is not easy to relate them to changes in the matter distribution, which can be significant, particularly in the center of the nucleus.

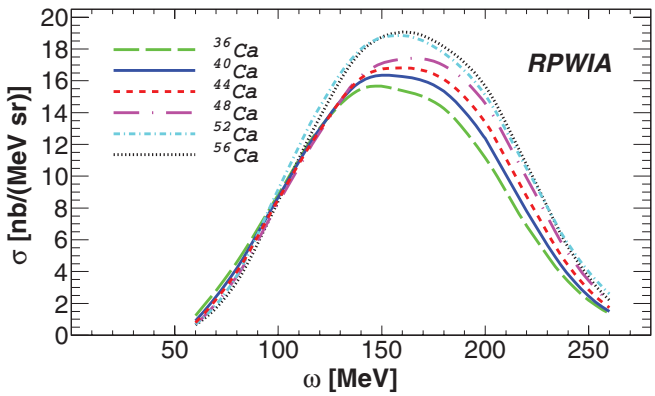

FIG. 9. (Color online) Differential RPWIA cross section for the inclusive QE (e, e') reaction on $^{36-56}$Ca at $\varepsilon = 560$ MeV and $\theta = 60^\circ$ as a function of ω.

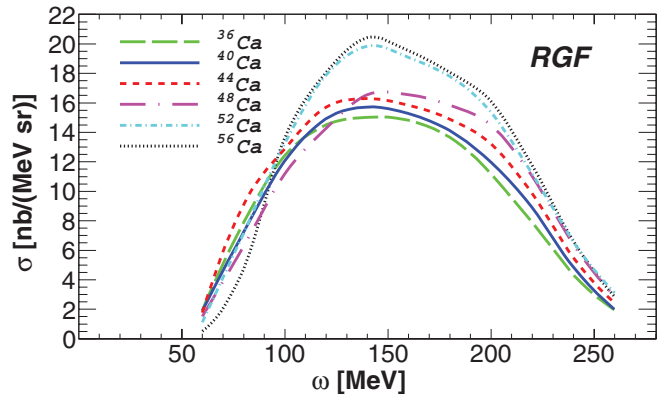

FIG. 10. (Color online) The same as in Fig. 9, but in the RGF model.

C. Parity-violating asymmetry

The calculation starts with the self-consistent relativistic ground-state proton and neutron densities (see Sec. III). The charge and weak densities are calculated by folding the point proton and neutron densities [see Eq. (10)]. The resulting Coulomb potential $V(r)$ and weak potential $A(r)$ [see Eq. (9)] are used to construct $U_\pm(r)$. The cross sections for elastic electron scattering are obtained from the numerical solution of the Dirac equation for electron scattering in the $U_\pm(r)$ potential and includes Coulomb distortion effects [36,51,56,109]. The cross sections for positive and negative helicity electron states are calculated and the resulting asymmetry parameter A_{pv} is plotted as a function of the scattering angle.

In Figs. 11 and 12 we plot the parity-violating asymmetry parameters A_{pv} for $^{14-28}$O and $^{36-56}$Ca nuclei for elastic electron scattering at $\varepsilon = 850$ MeV. At $\varepsilon = 850$ MeV the values of A_{pv} are of the order of 10^{-5}, with lower values for smaller angles and larger values for larger angles.

As suggested in Ref. [49] the asymmetry parameter A_{pv} provides a direct measurement of the Fourier transform of the neutron density. This relation has been tested and confirmed in Ref. [60] comparing asymmetries and the squares of the

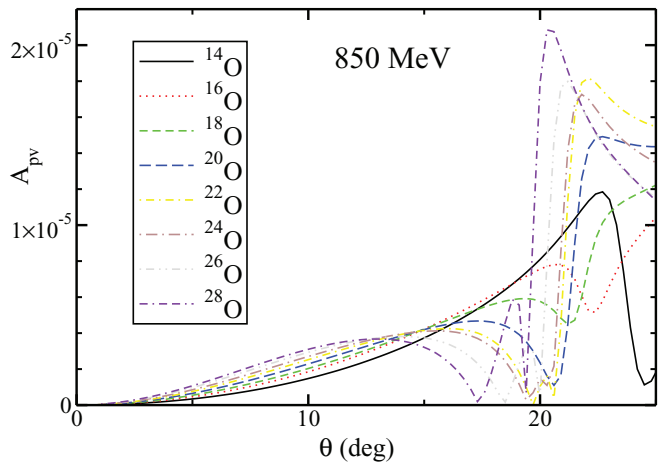

FIG. 11. (Color online) Parity-violating asymmetry parameter A_{pv} for elastic electron scattering at $\varepsilon = 850$ MeV as function of the scattering angle θ on $^{14-28}$O.

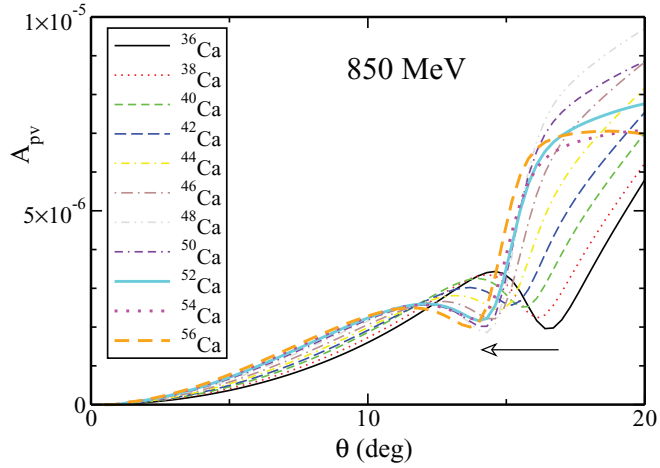

FIG. 12. (Color online) The same as in Fig. 11, but for $^{36-56}$Ca. The black arrow emphasizes the evolution of A_{pv} as a function of the neutron number N.

Fourier transforms of the neutron densities. Another way to relate A_{pv} to neutron distributions of finite nuclei is by looking at possible linear correlations between the asymmetry parameter and some well defined observables. We suggest to use the first minima positions θ_{min} and the neutron excess $\Delta = \frac{N-Z}{Z}$, i.e., how the minima of A_{pv} evolve from neutron-poor to neutron-rich nuclei [see Eqs. (13) and (14)]. In Fig. 13, θ_{min} is plotted as a function of Δ for oxygen and calcium isotopes. The dashed lines suggest that for both isotope chains the evolution of A_{pv} as a function of Δ is well approximated by a linear fit with a very similar slope. To test the robustness of this correlation it is interesting to study if A_{pv} is affected by density distribution oscillations at small radii that could appear in some selected cases. In Ref. [39], ^{22}O and ^{24}O isotopes have been studied as possible candidates for "bubble" nuclei, i.e., nuclear systems with a strong depleted central density. In Fig. 14 we plot the asymmetry parameters A_{pv} for these nuclei. Neutron density profiles show large differences at small distances.

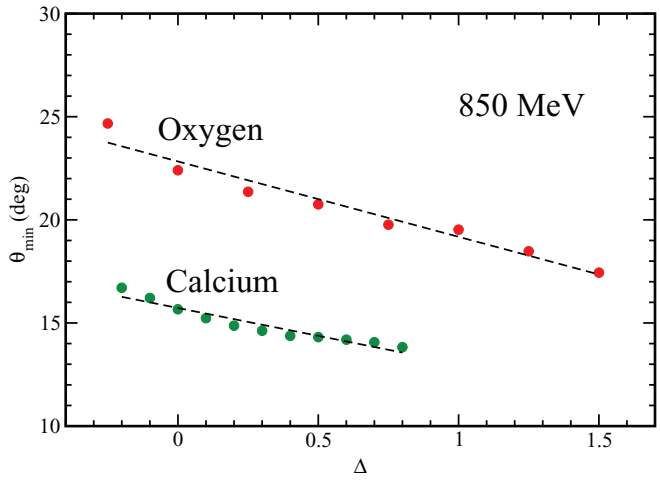

FIG. 13. (Color online) First minimum positions of the asymmetry parameter A_{pv} as functions of $\Delta = (N - Z)/Z$ for $^{14-28}$O and $^{36-56}$Ca. The black dashed lines represent the best linear fit.

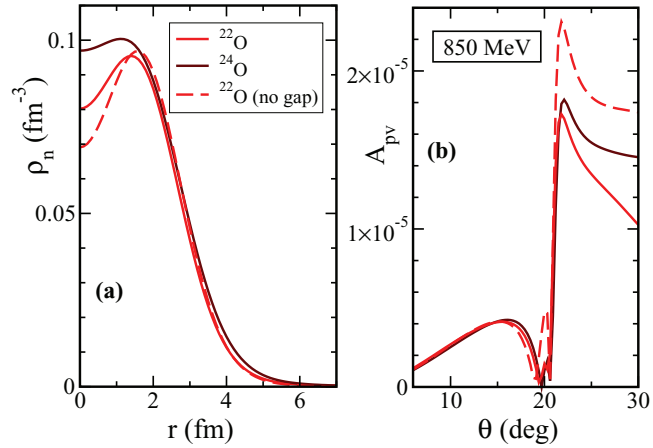

FIG. 14. (Color online) (a) Neutron density distributions for some selected nuclei (^{22}O and ^{24}O) that could be interpreted as candidates for "bubble" structure [39]. (b) Parity-violating asymmetry parameter A_{pv} for elastic electron scattering at $\varepsilon = 850$ MeV as a function of the scattering angle θ.

No appreciable effects are obtained in the corresponding asymmetries up to $\theta \simeq 20^{\circ}$; then for larger scattering angles the asymmetries are sensitive to the differences in the density distributions and are significantly different. Therefore, A_{pv} is still a reliable observable to study neutron radii even if we include pairing correlations, but we must limit to angles smaller than the first minimum position.

In addition to predictions about oxygen and calcium isotopic chains we also provide calculations for recent measurements and future experiments. In Fig. 15 we show our

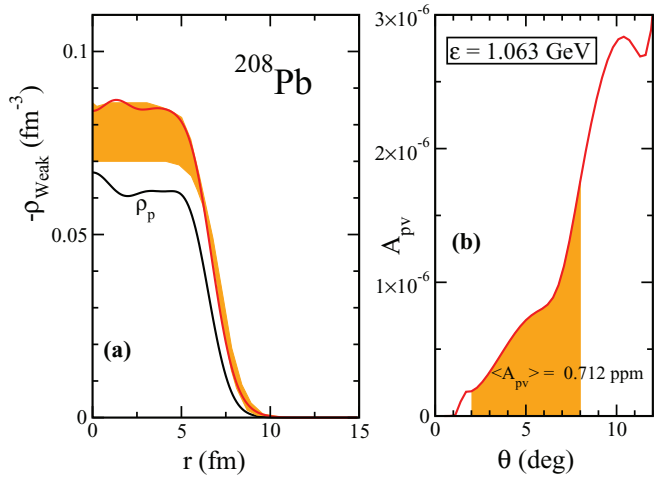

FIG. 15. (Color online) (a) Theoretical weak charge density (red line) in comparison with the experimental error band as determined in Ref. [53] for ^{208}Pb with the kinematics of the PREX experiment. The corresponding proton density profile is plotted with a black line. (b) Asymmetry parameter for ^{208}Pb as a function of the angle θ (red line). The shaded area represents the interval covered by the acceptance function $\epsilon(\theta)$ (see Ref. [52] for more details). The asymmetry parameter averaged over the acceptance $\langle A_{pv} \rangle$ is in quite good agreement with the empirical value 0.656 ± 0.060 (stat) $\pm$ 0.014 (syst) ppm.

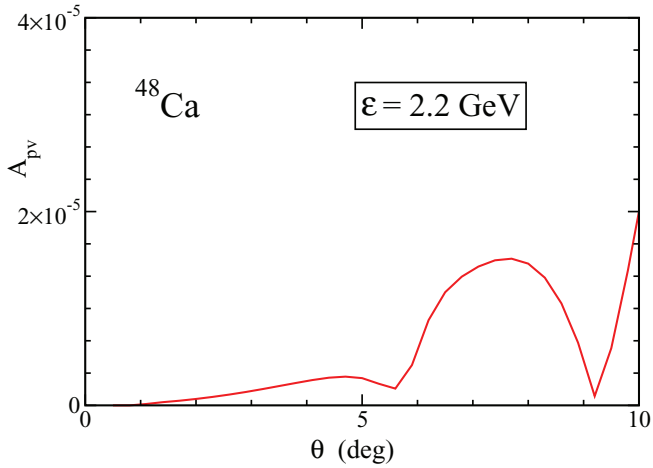

FIG. 16. (Color online) Parity-violating asymmetry parameters $A_{\rm pv}$ for elastic electron scattering at $\varepsilon = 2.2$ GeV as a function of the scattering angle θ for ^{48}Ca; see Ref. [55].

theoretical predictions for the empirical values extracted from the first run of the PREX experiment on ^{208}Pb at $\varepsilon = 1.06$ GeV. In Ref. [53] the weak charge density $(-\rho_W)$ has been deduced from the weak charge form factor. The error band (shaded area) represents the incoherent sum of experimental and model errors. Our prediction, plotted by the red line in the left panel, is in rather good agreement with empirical data. In fact, if we evaluate the corresponding asymmetry parameter $A_{\rm pv}$ averaged over the acceptance function $\epsilon(\theta)$ [110],

$$\langle A_{\rm pv}\rangle = \frac{\int {\rm d}\theta \sin\theta A_{\rm pv}(\theta)\frac{d\sigma}{d\Omega}\epsilon(\theta)}{\int {\rm d}\theta \sin\theta \frac{d\sigma}{d\Omega}\epsilon(\theta)}, \qquad (27)$$

we find 0.712 ppm, in very good agreement with the empirical estimate 0.656 ± 0.060 (stat) ± 0.014 (syst) ppm. In Fig. 16 we calculate the asymmetry parameter for ^{48}Ca with 2.2-GeV electrons as planned for the CREX experiment. For energies well above the 1-GeV region, of course, the elastic scattering approximation is not completely under control and corrections owing to possible inelasticities should be taken into account. We plan to extend our calculation in a forthcoming paper.

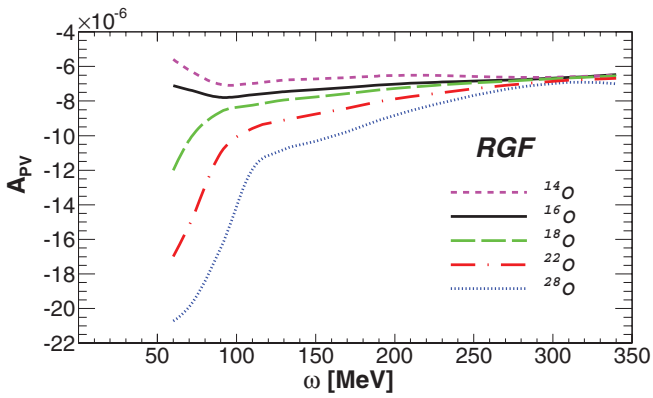

FIG. 17. (Color online) Parity-violating asymmetry for the QE (e, e') reaction on O isotopes with the RGF for $\varepsilon = 1080$ MeV and $\theta = 32^\circ$.

As an example of the parity-violating asymmetry for QE scattering, in Fig. 17 we show $A_{\rm pv}$ for the ^{14,16,18,22,28}O isotopes evaluated with the RGF in the same kinematics as in Fig. 8. Note that the results are rescaled by the factor 10^5. The RPWIA results are always similar to the RGF ones and are not presented here. The asymmetry is almost constant to a few $\times 10^{-6}$ for ^{14}O and ^{16}O, whereas for ^{22}O and ^{28}O it goes up to $\approx -2 \times 10^{-5}$ in the low energy transferred region. There are visible relative differences between the asymmetries for the oxygen isotopes that we have considered, but we are aware that a measurement of $A_{\rm pv}$ in QE electron scattering off finite nuclei is extremely challenging with the presently available facilities.

VI. SUMMARY AND CONCLUSIONS

We have presented and discussed numerical predictions for the cross section and the parity-violating asymmetry in elastic and QE electron scattering on oxygen and calcium isotope chains with the aim of investigating their evolution with increasing neutron number.

The understanding of the properties of exotic nuclei is one of the major topics of interest in modern nuclear physics. Large efforts in this direction have been done over recent years and are planned for the future. The use of electrons as probes provides a powerful tool for achieving this goal. The RIB facilities in different laboratories have opened the possibility to give insight into nuclear structures that are not available in nature, as they are not stable, but which are important in astrophysics and had a relevant role in the nucleosynthesis.

Electron scattering is well fitted for studying nuclear properties, as its interaction is well known and relatively weak with respect to the hadron force and can therefore more adequately explore the details of inner nuclear structures. As a consequence of this weakness, the cross sections become very small and more difficult experiments have to be performed. Electron scattering experiments off exotic nuclei have been proposed in the ELISe experiment at FAIR and in the SCRIT project at RIKEN. We hope that the existing proposals will be considered and approved in the coming years. Our theoretical predictions will be useful for clarifying the different aspects of the measurements, giving information on the order of magnitude of the measurable quantities and therefore making possible a more precise evaluation of the experimental difficulties. Moreover, a theoretical investigation can be helpful to envisage the most interesting quantities to be measured to explore the properties of exotic nuclear structures.

In this work, both elastic and inclusive QE electron scattering have been considered. The elastic scattering can give information on the global properties of nuclei and, in particular, on the different behavior of proton and neutron density distributions. The inclusive QE scattering is affected by the dynamical properties, being the integral of the spectral density function over all the available final states and, owing to the reaction mechanism, preferably exploits the s.p. aspects of the nucleus. In addition, when combined with the exclusive $(e, e'p)$ scattering, it is able to explore the evolution of the s.p. model with increasing asymmetry between the number of neutrons and protons. Many interesting phenomena are

predicted in this situation, in particular, the modification of the shell model magic numbers. A definite response can be obtained from the comparison with experimental data, which will discriminate between the different theoretical models, mainly referring to RMF approaches.

As case studies for the present investigation we have selected oxygen and calcium isotope chains. The calculations have been carried out within the framework of the RMF model. The nuclear wave functions are obtained considering a system of nucleons coupled to the exchange mesons and the electromagnetic field through an effective Lagrangian. The calculated cross sections include both the hadronic and the Coulomb final-states interactions. The inclusive QE scattering is calculated with the RGF model, which conserves the global particle flux in all the final state channels, as is required in an inclusive reaction.

First, the models have been compared with experimental data already available on stable isotopes to check their reliability. Then, the same models have been used to calculate elastic and inclusive QE cross sections on exotic isotope chains. The possible disagreement of the experimental findings from the theoretical predictions will be a clear indication of the insurgence of new phenomena related to the proton to neutron asymmetry.

Our results show an evolution of the calculated quantities without discontinuities. The increase of the neutron number essentially produces an increase of the nuclear and proton densities and a flattening of the charge density.

The parity-violating asymmetry parameter has been calculated to investigate the neutron skin, as the weak current is essentially obtained from the interaction with neutrons. Numerical predictions have been presented and discussed for oxygen and calcium isotopes. Moreover, we have compared our calculations with the results of the first measurement of the asymmetry parameter achieved by the PREX Collaboration on ^{208}Pb and have obtained a good agreement with the empirical value. A prediction for the future experiment CREX on ^{48}Ca has also been given.

ACKNOWLEDGMENTS

This work was partially supported by the Italian MIUR through the PRIN 2009 research project.

[1] R. Hofstadter, Rev. Mod. Phys. **28**, 214 (1956).
[2] T. W. Donnelly and J. D. Walecka, Annu. Rev. Nucl. Part. Sci. **25**, 329 (1975).
[3] T. W. Donnelly and I. Sick, Rev. Mod. Phys. **56**, 461 (1984).
[4] S. Boffi, C. Giusti, and F. D. Pacati, Phys. Rep. **226**, 1 (1993).
[5] S. Boffi, C. Giusti, F. D. Pacati, and M. Radici, *Electromagnetic Response of Atomic Nuclei*, Oxford Studies in Nuclear Physics Vol. 20 (Clarendon Press, Oxford, 1996).
[6] O. Benhar, D. Day, and I. Sick, Rev. Mod. Phys. **80**, 189 (2008).
[7] H. De Vries, C. W. De Jager, and C. De Vries, At. Data Nucl. Data Tables **36**, 495 (1987).
[8] G. Fricke, C. Bernhardt, K. Heilig, L. A. Schaller, L. Schellenberg, E. B. Shera, and C. W. De Jager, At. Data Nucl. Data Tables **60**, 177 (1995).
[9] J. Heisenberg and H. P. Blok, Annu. Rev. Nucl. Part. Sci. **33**, 569 (1983).
[10] E. Moya de Guerra, Phys. Rep. **138**, 293 (1986).
[11] M. N. Harakeh and A. van der Woude, *Giant Resonances*, Oxford Studies in Nuclear Physics Vol. 24 (Clarendon Press, Oxford, 2001).
[12] S. Frullani and J. Mougey, Adv. Nucl. Phys. **14**, 1 (1984).
[13] M. Bernheim, A. Bussiere, J. Mougey, D. Royer, S. Tarnowski, D. Turck-Chièze, S. Frullani, S. Boffi, C. Giusti, and F. D. Pacati, Nucl. Phys. A **375**, 381 (1982).
[14] L. Lapikás, Nucl. Phys. A **553**, 297 (1993).
[15] P. K. A. de Witt Huberts, J. Phys. G **16**, 507 (1990).
[16] J. M. Udías, P. Sarriguren, E. Moya de Guerra, E. Garrido, and J. A. Caballero, Phys. Rev. C **48**, 2731 (1993).
[17] J. Gao *et al.* (The Jefferson Lab Hall A Collaboration), Phys. Rev. Lett. **84**, 3265 (2000).
[18] http://faculty.virginia.edu/qes-archive/index.html.
[19] I. Tanihata, Prog. Part. Nucl. Phys. **35**, 505 (1995).
[20] H. Geissel, G. Müzenberg, and R. Riisager, Annu. Rev. Nucl. Part. Sci. **45**, 163 (1995).
[21] A. Mueller, Prog. Part. Nucl. Phys. **46**, 359 (2001).
[22] T. Suda, K. Maruyama, and I. Tanhihata, RIKEN Accel. Prog. Rep. **34**, 49 (2001).
[23] T. Suda, M. Wakasugi, T. Emoto, K. Ishii, S. Ito, K. Kurita, A. Kuwajima, A. Noda, T. Shirai, T. Tamae, H. Tongu, S. Wang, and Y. Yano, Phys. Rev. Lett. **102**, 102501 (2009).
[24] T. Katayama, T. Suda, and I. Tanhihata, Phys. Scr., T **104**, 129 (2003).
[25] http://www-alt.gsi.de/documents/DOC-2006-Mar-118-1.pdf.
[26] http://www.gsi.de/forschung/fair_experiments/elise/index_e.html.
[27] H. Simon, Nucl. Phys. A **787**, 102 (2007).
[28] A. N. Antonov *et al.*, Nucl. Instrum. Methods A **637**, 60 (2011).
[29] T. Suda, Proposal for Nuclear Physics Experiments at RIBF NP1006-SCRIT01, 2010.
[30] T. Suda, T. Adachi, T. Amagai, A. Enokizono, M. Hara, T. Hori, S. Ichikawa, K. Kurita, T. Miyamoto, R. Ogawara, T. Ohnishi, Y. Shimakura, T. Tamae, M. Togasaki, M. Wakasugi, S. Wang, and K. Yanagi, Prog. Theor. Exp. Phys. **2012**, 03C008 (2012).
[31] E. Garrido and E. Moya de Guerra, Nucl. Phys. A **650**, 387 (1999).
[32] E. Garrido and E. Moya de Guerra, Phys. Lett. B **488**, 68 (2000).
[33] S. N. Ershov, B. V. Danilin, and J. S. Vaagen, Phys. Rev. C **72**, 044606 (2005).
[34] Z. Wang and Z. Ren, Phys. Rev. C **70**, 034303 (2004).
[35] A. N. Antonov, M. K. Gaidarov, D. N. Kadrev, P. E. Hodgson, and E. Moya de Guerra, Int. J. Mod. Phys. E **13**, 759 (2004).
[36] A. N. Antonov, D. N. Kadrev, M. K. Gaidarov, E. Moya de Guerra, P. Sarriguren, J. M. Udías, V. K. Lukyanov, E. V. Zemlyanaya, and G. Z. Krumova, Phys. Rev. C **72**, 044307 (2005).
[37] C. A. Bertulani, Phys. Rev. C **75**, 024606 (2007).
[38] E. Khan, M. Grasso, J. Margueron, and N. Van Giai, Nucl. Phys. A **800**, 37 (2008).

[39] M. Grasso, L. Gaudefroy, E. Khan, T. Nikšić, J. Piekarewicz, O. Sorlin, N. Van Giai, and D. Vretenar, Phys. Rev. C **79**, 034318 (2009).
[40] Y. Chu, Z. Ren, T. Dong, and Z. W. Wang, Phys. Rev. C **79**, 044313 (2009).
[41] X. Roca-Maza, M. Centelles, F. Salvat, and X. Viñas, Phys. Rev. C **78**, 044332 (2008).
[42] X. Roca-Maza, M. Centelles, F. Salvat, and X. Viñas, Phys. Rev. C **87**, 014304 (2013).
[43] T. Dong, Y. Chu, Z. Ren, and Z. Wang, Phys. Rev. C **79**, 014317 (2009).
[44] T. Dong, Z. Ren, and Z. Wang, Phys. Rev. C **77**, 064302 (2008).
[45] J. Liu, Z. Ren, and T. Dong, Nucl. Phys. A **888**, 45 (2012).
[46] T. Dong, Y. Chu, and Z. Ren, J. Phys. Conf. Ser. **381**, 012135 (2012).
[47] C. Giusti, A. Meucci, F. D. Pacati, G. Co', and V. De Donno, Phys. Rev. C **84**, 024615 (2011).
[48] G. Co', V. De Donno, P. Finelli, M. Grasso, M. Anguiano, A. M. Lallena, C. Giusti, A. Meucci, and F. D. Pacati, Phys. Rev. C **85**, 024322 (2012).
[49] T. W. Donnelly, J. Dubach, and I. Sick, Nucl. Phys. A **503**, 589 (1989).
[50] T. W. Donnelly and R. D. Peccei, Phys. Rep. **50**, 1 (1979).
[51] C. J. Horowitz, Phys. Rev. C **57**, 3430 (1998).
[52] S. Abrahamyan *et al.* (PREX Collaboration), Phys. Rev. Lett. **108**, 112502 (2012).
[53] C. J. Horowitz, Z. Ahmed, C. M. Jen, A. Rakhman, P. A. Souder, M. M. Dalton, N. Liyanage, K. D. Paschke, K. Saenboonruang, R. Silwal, G. B. Franklin, M. Friend, B. Quinn, K. S. Kumar, D. McNulty, L. Mercado, S. Riordan, J. Wexler, R. W. Michaels, and G. M. Urciuoli, Phys. Rev. C **85**, 032501 (2012).
[54] PREX-II, Proposal to Jefferson Lab PAC 38, http://hallaweb.jlab.org/parity/prex/prexII.pdf.
[55] Proposal to Jefferson Lab PAC 39, http://hallaweb.jlab.org/parity/prex.
[56] O. Moreno, P. Sarriguren, E. Moya de Guerra, J. M. Udías, T. W. Donnelly, and I. Sick, Nucl. Phys. A **828**, 306 (2009).
[57] S. Ban, C. J. Horowitz, and R. Michaels, J. Phys. G: Nucl. Part. Phys. **39**, 015104 (2012).
[58] X. Roca-Maza, M. Centelles, X. Viñas, and M. Warda, Phys. Rev. Lett. **106**, 252501 (2011).
[59] E. Moya de Guerra, O. Moreno, P. Sarriguren, and M. Ramon, J. Phys.: Conf. Ser. **366**, 012011 (2012).
[60] D. Vretenar, P. Finelli, A. Ventura, G. A. Lalazissis, and P. Ring, Phys. Rev. C **61**, 064307 (2000).
[61] C. J. Horowitz, S. J. Pollock, P. A. Souder, and R. Michaels, Phys. Rev. C **63**, 025501 (2001).
[62] P. Finelli, N. Kaiser, D. Vretenar, and W. Weise, Nucl. Phys. A **735**, 449 (2004).
[63] P. Finelli, N. Kaiser, W. Weise, and D. Vretenar, in *Theoretical Nuclear Physics in Italy*, edited by S. Boffi, A. Covello, M. Di Toro, A. Fabrocini, G. Pisent, and S. Rosati (World Scientific, Singapore, 2004), Chap. 5, pp. 45–52.
[64] P. Finelli, N. Kaiser, D. Vretenar, and W. Weise, Nucl. Phys. A **770**, 1 (2006).
[65] C. Fuchs, H. Lenske, and H. H. Wolter, Phys. Rev. C **52**, 3043 (1995).
[66] S. Typel and H. H. Wolter, Nucl. Phys. A **656**, 331 (1999).
[67] T. Nikšić, D. Vretenar, P. Finelli, and P. Ring, Phys. Rev. C **66**, 024306 (2002).
[68] G. A. Lalazissis, T. Nikšić, D. Vretenar, and P. Ring, Phys. Rev. C **71**, 024312 (2005).
[69] D. Vretenar, A. V. Afanasjev, G. A. Lalazissis, and P. Ring, Phys. Rep. **409**, 101 (2005).
[70] A. Meucci, F. Capuzzi, C. Giusti, and F. D. Pacati, Phys. Rev. C **67**, 054601 (2003).
[71] A. Meucci, C. Giusti, and F. D. Pacati, Nucl. Phys. A **739**, 277 (2004).
[72] A. Meucci, C. Giusti, and F. D. Pacati, Nucl. Phys. A **756**, 359 (2005).
[73] A. Meucci, J. A. Caballero, C. Giusti, F. D. Pacati, and J. M. Udías, Phys. Rev. C **80**, 024605 (2009).
[74] A. Meucci, J. A. Caballero, C. Giusti, and J. M. Udías, Phys. Rev. C **83**, 064614 (2011).
[75] A. Meucci and C. Giusti, Phys. Rev. D **85**, 093002 (2012).
[76] A. Meucci, C. Giusti, and F. D. Pacati, Phys. Rev. D **84**, 113003 (2011).
[77] A. Meucci, M. B. Barbaro, J. A. Caballero, C. Giusti, and J. M. Udías, Phys. Rev. Lett. **107**, 172501 (2011).
[78] C. Giusti, A. Meucci, F. D. Pacati, G. Co', and V. De Donno, J. Phys.: Conf. Ser. **366**, 012019 (2012).
[79] O. Moreno, P. Sarriguren, E. Moya de Guerra, J. M. Udías, T. W. Donnelly, and I. Sick, J. Phys.: Conf. Ser. **312**, 092044 (2011).
[80] P. Moller and J. R. Nix, Nucl. Phys. A **536**, 20 (1992).
[81] A. Schiller, T. Baumann, J. Dietrich, S. Kaiser, W. Peters, and M. Thoennessen, Phys. Rev. C **72**, 037601 (2005).
[82] A. Meucci, C. Giusti, and F. D. Pacati, Phys. Rev. C **64**, 014604 (2001).
[83] A. Meucci, C. Giusti, and F. D. Pacati, Phys. Rev. C **64**, 064615 (2001).
[84] A. Meucci, Phys. Rev. C **65**, 044601 (2002).
[85] M. Radici, A. Meucci, and W. H. Dickhoff, Eur. Phys. J. A **17**, 65 (2003).
[86] T. Tamae, Y. Sato, T. Yokokawa, Y. Asano, M. Kawabata, O. Konno, I. Nakagawa, I. Nishikawa, K. Hirota, H. Yamazaki, R. Kimura, H. Miyase, H. Tsubota, C. Giusti, and A. Meucci, Phys. Rev. C **80**, 064601 (2009).
[87] C. Maieron, M. C. Martinez, J. A. Caballero, and J. M. Udías, Phys. Rev. C **68**, 048501 (2003).
[88] A. Meucci, C. Giusti, and F. D. Pacati, Nucl. Phys. A **744**, 307 (2004).
[89] A. Meucci, C. Giusti, and F. D. Pacati, Acta Phys. Polon. B **37**, 2279 (2006).
[90] A. Meucci, C. Giusti, and F. D. Pacati, Nucl. Phys. A **773**, 250 (2006).
[91] J. A. Caballero, Phys. Rev. C **74**, 015502 (2006).
[92] A. Meucci, C. Giusti, and F. D. Pacati, Phys. Rev. C **77**, 034606 (2008).
[93] C. Giusti, A. Meucci, and F. D. Pacati, Acta Phys. Pol. B **40**, 2579 (2009).
[94] J. A. Caballero, M. C. Martinez, J. L. Herraiz, and J. M. Udías, Phys. Lett. B **688**, 250 (2010).
[95] A. V. Butkevich, Phys. Rev. C **82**, 055501 (2010).
[96] A. V. Butkevich, Phys. Rev. C **85**, 065501 (2012).
[97] F. Capuzzi, C. Giusti, and F. D. Pacati, Nucl. Phys. A **524**, 681 (1991).
[98] F. Capuzzi, C. Giusti, F. D. Pacati, and D. N. Kadrev, Ann. Phys. (NY) **317**, 492 (2005).
[99] Brookhaven National Laboratory-National Nuclear Data Center, http://www.nndc.bnl.gov/.

[100] P. Sarriguren, M. K. Gaidarov, E. M. de Guerra, and A. N. Antonov, Phys. Rev. C **76**, 044322 (2007).
[101] Z. Wang and Z. Ren, Phys. Rev. C **71**, 054323 (2005).
[102] E. D. Cooper, S. Hama, and B. C. Clark, Phys. Rev. C **80**, 034605 (2009).
[103] T. de Forest, Jr., Nucl. Phys. A **392**, 232 (1983).
[104] M. Anghinolfi, M. Battaglieri, N. Bianchi, R. Cenni, P. Corvisiero, A. Fantoni, P. Levi Sandri, A. Longhi, V. Lucherini, V. I. Mokeev, V. Muccifora, E. Polli, A. Reolon, G. Ricco, M. Ripani, P. Rossi, S. Simula, M. Taiuti, A. Teglia, and A. Zucchiatti, Nucl. Phys. A **602**, 405 (1996).
[105] C. F. Williamson, T. C. Yates, W. M. Schmitt, M. Osborn, M. Deady, P. D. Zimmerman, C. C. Blatchley, K. K. Seth, M. Sarmiento, B. Parker, Y. Jin, L. E. Wright, and D. S. Onley, Phys. Rev. C **56**, 3152 (1997).
[106] M. B. Barbaro, J. A. Caballero, T. W. Donnelly, and C. Maieron, Phys. Rev. C **69**, 035502 (2004).
[107] J. E. Amaro, M. B. Barbaro, J. A. Caballero, T. W. Donnelly, A. Molinari, and I. Sick, Phys. Rev. C **71**, 015501 (2005).
[108] M. V. Ivanov, M. B. Barbaro, J. A. Caballero, A. N. Antonov, E. Moya de Guerra, and M. K. Gaidarov, Phys. Rev. C **77**, 034612 (2008).
[109] G. Rufa, Nucl. Phys. A **384**, 273 (1982).
[110] See Supplemental Material to Ref. [52] at http://prl.aps.org/supplemental/PRL/v108/i11/e112502 for the acceptance function $\epsilon(\theta)$ to be used in Eq. (3) of Ref. [52].
[111] B. B. P. Sinha, G. A. Peterson, R. R. Whitney, I. Sick, and J. S. McCarthy, Phys. Rev. C **7**, 1930 (1973).
[112] I. Sick and J. S. McCarthy, Nucl. Phys. A **150**, 631 (1970).